# Kinematic dynamo action of a precession driven flow based on the results of water experiments and hydrodynamic simulations

Giesecke, A.; Vogt, T.; Gundrum, T.; Stefani, F.;

# Kinematic dynamo action of a precession driven flow based on the results of water experiments and hydrodynamic simulations.

André Giesecke[*], Tobias Vogt, Thomas Gundrum, and Frank Stefani

Helmholtz-Zentrum Dresden-Rossendorf, Bautzner Landstrasse 400, D-01328 Dresden, Germany

The project DRESDYN (DREsden Sodium facility for DYNamo and thermohydraulic studies) conducted at Helmholtz-Zentrum Dresden-Rossendorf (HZDR) provides a new platform for a variety of liquid sodium experiments devoted to problems of geo- and astrophysical magnetohydrodynamics. The most ambitious experiment within this project is a precession driven dynamo experiment that currently is under construction. It consists of a cylinder filled with liquid sodium that simultaneously rotates around two axes. The experiment is motivated by the idea of a precession-driven flow as a complementary energy source for the geodynamo or the ancient lunar dynamo.

In the present study we address numerical and experimental examinations in order to identify parameter regions where the onset of magnetic field excitation will be most probable. Both approaches show that in the strongly nonlinear regime the flow is essentially composed of the directly forced primary Kelvin mode and higher modes in terms of standing inertial waves that arise from nonlinear self-interactions. A peculiarity is the resonance-like emergence of an axisymmetric mode that represents a double roll structure in the meridional plane, which, however, only occurs in a very limited range of the precession ratio. This axisymmetric mode turns out to be beneficial for dynamo action, and kinematic simulations of the magnetic field evolution induced by the time-averaged flow exhibit magnetic field excitation at critical magnetic Reynolds numbers around $\mathrm{Rm}^c \approx 430$, which is well within the range of the planned liquid sodium experiment.

**Keywords:** Dynamo, Rotating Fluids

## 1. Introduction

Precession driven flows are found in technical applications, e.g. in flying and rotating objects with liquid payloads (spacecrafts, rockets, satellites), as well as in geophysical problems, like cyclonic structures in the Earths atmosphere that form hurricanes or tornados. Precession driven flows are also relevant in the liquid part of the Earth's core (Stewartson and Roberts 1963), which more than 100 years ago was already a motivation for the pioneering study of Henri Poincaré, who showed that the inviscid base flow in a precessing spheroid is described by a constant vorticity solution, the spin-over mode (Poincaré 1910). The extension of the calculation to the weakly nonlinear regime including thin boundary layers yields the Busse solution which describes the orientation of the effective rotation axis of the fluid (Busse 1968). Early experiments showed that precession is an efficient mechanism to drive a flow in a rotating container and provides powerful flows on the laboratory scale without making use of propellers or pumps (Léorat *et al.* 2003, Léorat 2006). In this context it is often speculated whether the Earth's magnetic field or the ancient magnetic field of the moon were powered by a flow driven by precession instead of or in addition to convection (Malkus 1968, Vanyo 1991, Noir and Cébron 2013). Dynamos generated by mechanical driving such as precession or tidal forcing have become popular in recent years, and experiments focussing on precession driven flows were conducted in various labs (McEwan 1970, Gans 1970, Vanyo and Likins 1971,

---

Manasseh 1992, Kobine 1995, 1996, Noir *et al.* 2001a, 2003, Goto *et al.* 2007, Lagrange *et al.* 2011, Mouhali *et al.* 2012, Lin *et al.* 2014, Herault *et al.* 2015, Horimoto and Goto 2017).

At Helmholtz-Zentrum Dresden-Rossendorf (HZDR) a dynamo experiment is presently under construction in which a precessing flow of liquid sodium is used in order to excite dynamo action (Stefani *et al.* 2012). The experiment consists of a cylinder with radius $R = 1$ m and height $H = 2$ m that will rotate around its symmetry axis with a frequency of up to $f_{\mathrm{c}} = 10$ Hz and precess around a second axis with up to $f_{\mathrm{p}} = 1$ Hz (figure 1). A cylindrical geometry has been chosen because the pressure forces that arise in the corners at the end caps provide a more efficient transfer of kinetic energy into the fluid compared to the spherical case where this only happens by viscous coupling at the walls. The device represents a considerably enlarged version of the liquid metal experiment conducted by Gans (1971) who achieved an amplification of an applied magnetic field by a factor of 3. However, in these experiments, the cylindrical container was far to small ($R = 0.125$ m) to provide a sufficiently large magnetic Reynolds number required for the onset of dynamo action.
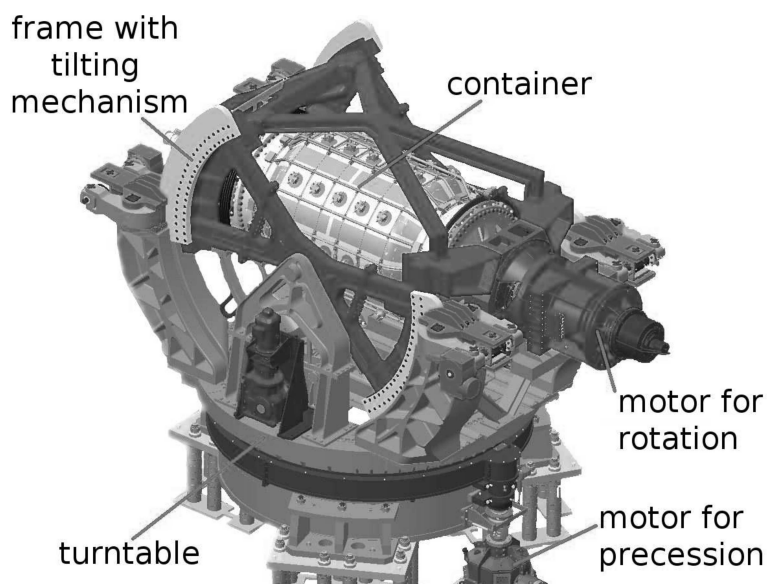


Figure 1.   Sketch of the planned precession experiment. The container (central cylinder) with a height and diameter of 2 m will rotate with up to 10 Hz. The device is mounted on a turntable that in turn can rotate with up to 1Hz. The angle between rotation axis and precession axis, i.e., the nutation angle, can be varied from $\alpha = 45°$ to $\alpha = 90°$ (Figure courtesy SBS Bühnentechnik GmbH).

First water test-experiments at HZDR focussing on the mechanical stability of the device and on the properties of the flow are scheduled for late 2019. In the very dynamo runs the cylinder will be filled with liquid sodium which is the best known liquid conductor. The typical critical magnetic Reynolds number that will be achievable in the dynamo experiment will be around $\mathrm{Rm} = \Omega_{\mathrm{c}} R^2/\eta \approx 700$ where $\Omega_{\mathrm{c}} = 2\pi f_{\mathrm{c}}$ is the angular frequency of the rotation of the cylinder and $\eta \approx 0.1$ m$^2$/s is the magnetic diffusivity of liquid sodium at a temperature of $T \approx 120°$ C.

The present study is an extension of the results presented in Giesecke *et al.* (2018). Here we detail numerical and experimental investigations of the hydrodynamics of a precession driven flow. Subsequently, the resulting flow data are applied to kinematic dynamo models which are conducted in preparation of the large scale experiment in order to estimate the parameter regimes that may be suited for the onset of dynamo action. Based on the growth rates for the magnetic field energy obtained for different velocity fields, we explicitly show that a dynamo occurs at experimentally attainable rotation and precession frequencies, although only in a very narrow regime. In addition to our previous results, we examine the impact of a

more realistic numerical set-up that considers an outer wall with finite thickness with a finite electrical conductivity that differs from the conductivity of the fluid in the interior.

The hydrodynamic water experiments are conducted with a down-scaled device with the same aspect ratio $\Gamma = H/R = 2$ as in the planned large scale facility. The experiment has been in operation at HZDR for several years to provide detailed information on the flow behavior in dependence of the rotation rate parameterized by the Reynolds number $Re = \Omega_c R^2/\nu$ and the precession ratio Po $= \Omega_p/\Omega_c$ with $\nu$ the viscosity and $\Omega_p = 2\pi f_p$ the angular frequency of the precession. Note that water has similar density and viscosity as liquid sodium so that the resulting outcome can well be applied for scaling to the flow behavior in the large scale liquid sodium device.
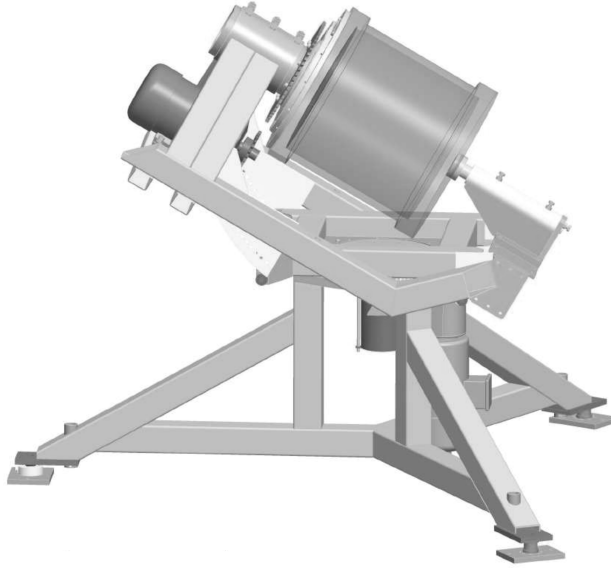


Figure 2.   Sketch of the water experiment. Compared to the planned large scale experiment the water device is smaller by a factor of 6.

It is well-known that a fluid flow forced by precession is instable (Kerswell 1993) and allows complex three-dimensional velocity structures that ultimately may end in a fully turbulent state. Such instabilities in precession driven flows have been found in experiments and simulations (Noir *et al.* 2003, Hollerbach and Kerswell 1995, Noir *et al.* 2001a, Lorenzani and Tilgner 2001, 2003, Noir *et al.* 2001b, Goto *et al.* 2014, Horimoto *et al.* 2018). Moreover, simulations in various geometries (spherical, ellipsoidal, cylindrical and cubic) have shown that the precession driven generation of magnetic fields is possible with a critical magnetic Reynolds number $Rm^c \sim O(10^3)$ (Tilgner 2005, Ernst-Hullermann *et al.* 2011, Wu and Roberts 2009, Lin *et al.* 2016, Goepfert and Tilgner 2016, Nore *et al.* 2011), which has strongly encouraged the construction of our precession dynamo experiment.

The preliminary experimental investigations are accompanied by hydrodynamic simulations with the code `SEMTEX` that applies quadrilateral spectral elements for the direct numerical simulation of the incompressible Navier Stokes equation (Blackburn and Sherwin 2004)[1]. The code has been thoroughly validated against analytical solutions and shows an excellent

---

[1]The code including documentation and examples is available at `http://users.monash.edu.au/~bburn/semtex.html`.

agreement with experimental data (see below). The two complementary approaches provide extensive information about the flow in the precessing cylinder and thus allow an estimation of the system's capability to obtain dynamo action in the planned large scale sodium device. For this purpose, the flow fields obtained in the hydrodynamic simulations serve as input for kinematic dynamo simulations that allow an assessment in which parameter ranges the occurrence of dynamo action is most likely.

The present paper is organized as follows: In the next section we briefly describe the theory and give a qualitative overview about the various characteristics of a precession driven flow in different regimes defined by the Poincaré number Po, i.e., the precession ratio (the ratio of precession frequency and the rotation frequency) $Po = \Omega_p/\Omega_c$.

The third section presents the results of the hydrodynamic experiment and simulations, which are applied in kinematic dynamo models that are detailed in the fourth section. In the final section we conclude our results and present an outlook for the large scale experiment.

## 2.   Inertial waves in a precessing fluid

In a precessing reference frame (we will call this in the following the mantle frame) the fluid flow is described by the Navier-Stokes equation including additional terms for a Coriolis force and the Poincaré force (Tilgner 1998):

$$\frac{\partial \boldsymbol{u}}{\partial t} + \boldsymbol{u}\cdot\boldsymbol{\nabla}\boldsymbol{u} \; = \; -\boldsymbol{\nabla}P \underbrace{-2(\boldsymbol{\Omega_p} + \boldsymbol{\Omega_c}) \times \boldsymbol{u}}_{\text{Coriolis force } \boldsymbol{F_c}} \underbrace{-(\boldsymbol{\Omega_p} \times \boldsymbol{\Omega_c}) \times \boldsymbol{r}}_{\text{Poincaré force } \boldsymbol{F_p}} + \nu\nabla^2\boldsymbol{u}\,. \tag{1}$$

Here $\boldsymbol{u}$ is the velocity field (obeying $\boldsymbol{\nabla}\cdot\boldsymbol{u} = 0$), $P$ the modified pressure (including the centrifugal terms), $\boldsymbol{\Omega_p}$ the angular frequency due to the precession, $\boldsymbol{\Omega_c}$ the angular frequency of the rotation of the container, and $\nu$ the viscosity. In the mantle frame $\boldsymbol{\Omega_p}$ is time dependent and given by

$$\boldsymbol{\Omega_p}(t) \; = \; \Omega_p\big[\sin\alpha\cos(\Omega_c t + \varphi)\hat{\boldsymbol{r}} \; - \; \sin\alpha\sin(\Omega_c t + \varphi)\hat{\boldsymbol{\varphi}} + \cos\alpha\hat{\boldsymbol{z}}\big]. \tag{2}$$

The Poincaré force on the right hand side of (1) results from the temporal change of the orientation of the rotation axis and provides a volume force that directly drives a fluid flow. In cylindrical systems the dynamical relevant part of this Poincaré force is

$$\boldsymbol{F_p} \; = \; -\Omega_c\Omega_p r\sin\alpha\cos(\Omega_c t + \varphi)\hat{\boldsymbol{z}} \tag{3}$$

with $\hat{\boldsymbol{z}}$ the unit vector along the rotation axis of the cylinder and $\alpha$ the nutation angle, i.e. the angle between precession axis and rotation axis. The spatial structure of the Poincaré force specifies the fundamental pattern of the directly driven flow which consists of a non-axisymmetric structure with the azimuthal wave number $m = 1$ ($\propto \cos\varphi$) and an odd axial wave number $k$, i.e., anti-symmetric with respect to the equatorial plane. In order to characterize the precession driven flow we utilize the eigenfunctions that result from the linear inviscid approximation. These solutions are inertial waves and read (Thomson 1880, Greenspan 1968)

$$\boldsymbol{U}_j(r, z, \varphi, t) \; = \; \boldsymbol{u}_j(r, z)e^{i(\omega_j t + m\varphi)} \; + \; \text{c.c.}, \tag{4}$$

where the single index $j$ comprises three numbers $m, k, n$, which denote the dependence on the azimuthal wave number $m$, the axial wave number $k$ and a third number $n$ that counts the roots of the dispersion relation. This dispersion relation determines the eigenfrequency of a Kelvin mode and reads

$$\omega_j\lambda_j \mathrm{J}_{m-1}(\lambda_j) + m\,(2 - \omega_j)\,\mathrm{J}_m(\lambda_j) \; = \; 0 \qquad \text{with} \qquad \omega_j = \pm 2\left[1 + \left(\frac{\lambda_j}{\Gamma k\pi}\right)^2\right]^{-1/2}, \tag{5a,b}$$

$J_m$ the Bessel function of order $m$, $\Gamma$ the aspect ratio defined by $\Gamma = H/R$ and $\lambda_j$ a radial wave number with its position in the sequence of zeros of (5a) corresponding to the number of half-cycles in the radial direction. An inertial mode becomes resonant when the frequency of the precession matches the natural frequency of the corresponding linear solution of the problem.

Experimental investigations have shown that the linear theory, which in addition to the structure of the main flow also allows the calculation of the associated amplitude, essentially provides a good representation of the observations when the nutation angle $\alpha$ remains small and the system is not close to a resonance of an inertial wave (Kobine 1995, Meunier *et al.* 2008). Linear corrections for the structure of inertial waves by viscous boundary layers were computed by Herreman (2009) for the simplified case of no-slip boundary conditions at the lateral cylinder walls whereas free-slip conditions were still assumed for the lids. A consideration of no-slip condition on all boundaries requires more complicated models, which, however, are only available for the directly driven $m = 1$ mode (Liao and Zhang 2012). In any case, even for small precession ratios nonlinear effects are important, which may trigger e.g. the resonant collapse, i.e., the breakdown of laminar-like structure into a chaotic flow observed repeatedly in precession experiments at small nutation angles $\alpha$ (McEwan 1970, Manasseh 1992, 1994), or the breaking of parity with respect to the equatorial plane (Tilgner 2005). Nonlinear self-interactions and viscous boundary layers will also be important for the planned experiment at HZDR with the aspect ratio $\Gamma = H/R = 2$ being close to the theoretical value $\Gamma = 1.9898174$ for the resonance of the simplest Kelvin mode with $m = 1$, $k = 1$ and $n = 1$. However, the corresponding nonlinear theory is a complex issue providing solutions only for particular conditions in the weakly nonlinear regime (Meunier *et al.* 2008, Lagrange *et al.* 2011). The difficulty for nonlinear models results from the suppression of nonlinear self-interactions of inertial modes at first order (Greenspan 1969) which hence must happen either at higher order, within the boundary layers (Busse 1968), or at internal singularities (Tilgner 2007). Nevertheless, it is precisely these interactions that are responsible for the major flow contributions beyond the directly forced mode and for the considerable modification of the azimuthal circulation (Kobine 1995) which is always oriented opposite to the (initial) solid body rotation, giving rise to a "braking" of the flow in the bulk of the cylinder. A direct consequence is the detuning of free inertial modes that appear in terms of triadic resonances (Giesecke *et al.* 2015, Lopez and Marques 2016, Herault *et al.* 2018, Albrecht *et al.* 2018) and the development of a strong shear layer in the vicinity of the lateral cylinder walls, which may become unstable provoking the abrupt transition into a turbulent flow regime if the forcing is sufficiently strong (Herault *et al.* 2015, Marques and Lopez 2015). Recent simulations have shown that such transient phenomena can indeed be explained by nonlinear models that involve a cascade of triadic resonances (Albrecht *et al.* 2018).

## 3.  The hydrodynamic flow in the water experiment

### 3.1.  *Setup*

Let us briefly describe the setup of the precession water experiment and the measurement techniques that are used to determine the flow structure and amplitude. The setup in the down-scaled water experiment consists of a cylindrical vessel having an inner length of $H = 326$ mm and an inner radius of $R = 163$ mm. Similar to the planned liquid sodium device, the down-scaled vessel can rotate with a maximum rotation rate of 10 Hz around its axis and is mounted on a turntable frame that allows for an additional rotation around a second axis with a maximum rotation rate of 1 Hz. The nutation angle between the two axes of rotation is kept at 90° throughout this study. One end wall of the vessel is equipped with 9 ultrasound transducers (TR0408SS, Signal Processing SA, Lausanne) whereby 6 transducers are arranged
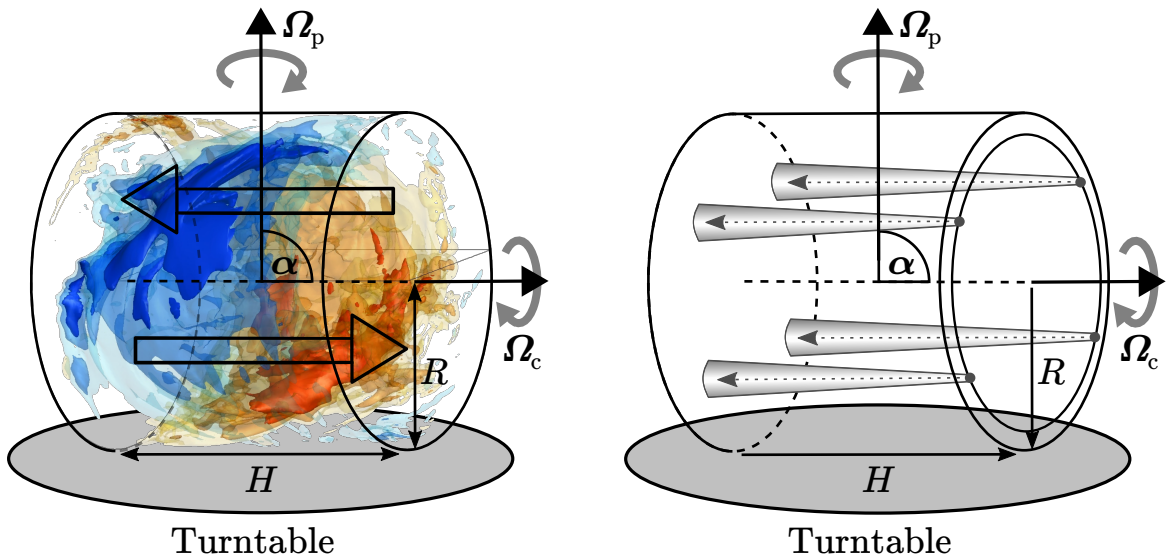
Figure 3.   Left: Flow field obtained from simulations at $Re = 10^4$ and $Po = 0.1$. The arrows denote the overall orientation of the axial velocity component (colour online). Right: sketch of the water experiment with four ultrasound probes mounted at one end cap of the cylinder.
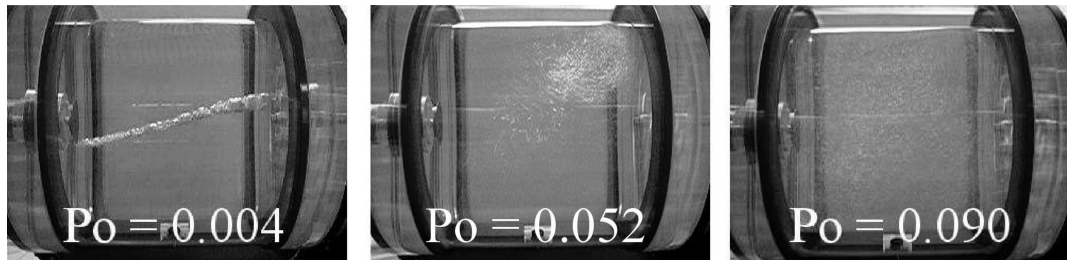


Figure 4.   Pictures of the flow behavior in three different regimes. The gas bubbles give an overall impression of the flow behavior. Left: Linear regime, weak precession ratios. Center: Nonlinear regime with large scale flow. Note the breaking of the equatorial symmetry. Right: Turbulent regime with no large scale structures recognizable in the dynamics of the bubbles.

in a radial array ranging from $r/R = 0$ to $0.92$, equally spaced. Four transducers are located at $r/R = 0.92$ having a $90°$ spacing in between in order to estimate the azimuthal symmetry of the flow. All transducers are aligned parallel to the vessel axis and capture the instantaneous axial velocity distribution between $z/H = 0$ and $1$. The transducers are connected to an ultrasound Doppler velocimeter (Dop 3010, Signal Processing SA, Lausanne) that records the velocity profiles with a temporal resolution of about 10 Hz.

### 3.2.    *Response of the fluid to precession*

We now discuss the behavior of the precession driven flow in the water experiment when the rotation rate remains fixed and the precession frequency is successively increased. A qualitative characterization of the flow behavior can easily be done by injecting a little amount of gas into the fluid and observing the distribution of the evolving gas bubbles within the precessing fluid. In the weekly precessing regime, these bubbles align along the minimum pressure line which follows an S-shaped tube that resembles the superposition of the nearly resonant forced mode and the solid body rotation thus indicating the effective fluid rotation axis (left panel in figure 4). In the intermediate range (approximately for $0.03 \lesssim Po \lesssim 0.06$) we observe a weakly nonlinear behavior characterized by erratic fluctuations of the minimum pressure line

(similar to the observations of Noir *et al.* 2003, in a precessing sphere) and by a breaking of the equatorial symmetry (central panel in figure 4). In this regime measurements of pressure fluctuations show periodic signatures that indicate the presence of two free Kelvin modes with azimuthal wave numbers $m = 5$ and $m = 6$ which constitute a triadic resonance with the forced mode (Herault *et al.* 2018). Triadic resonances have also been found in numerical simulations. However, since the Reynolds number in these computations is much lower, they are damped by viscous effects and could only be identified at aspect ratios away from the fundamental resonance (Giesecke *et al.* 2015) where detuning effects like those observed in Herault *et al.* (2018) are less significant. In all cases, in simulations as well as in experiments, the flow energy beyond the fundamental forced mode remains weak, and it seems to be rather difficult to inject kinetic energy in addition to the forced mode via a triadic resonance mechanism (Giesecke *et al.* 2015).

When attaining large precession ratios with Po $\gtrsim 0.07$, we ultimately observe an abrupt transition of the flow into a turbulent behavior with the large scale flow structures becoming less significant (right picture in figure 4). This transition becomes only evident at sufficiently fast rotation of the cylinder, i.e. at sufficiently large Re. At the rather low values for Re that can be achieved in our simulations (maximum value $\mathrm{Re} = 10^4$) or for which flow measurements are practicable with UDV (maximum value for reliable quantitative measurements $\mathrm{Re} = 10^5$) the flow maintains large scale structures for all precession ratios and the transition into the turbulent regime characterized in Herault *et al.* (2015) can only be identified by secondary criteria, like the abrupt drop of the amplitude of the forced mode.
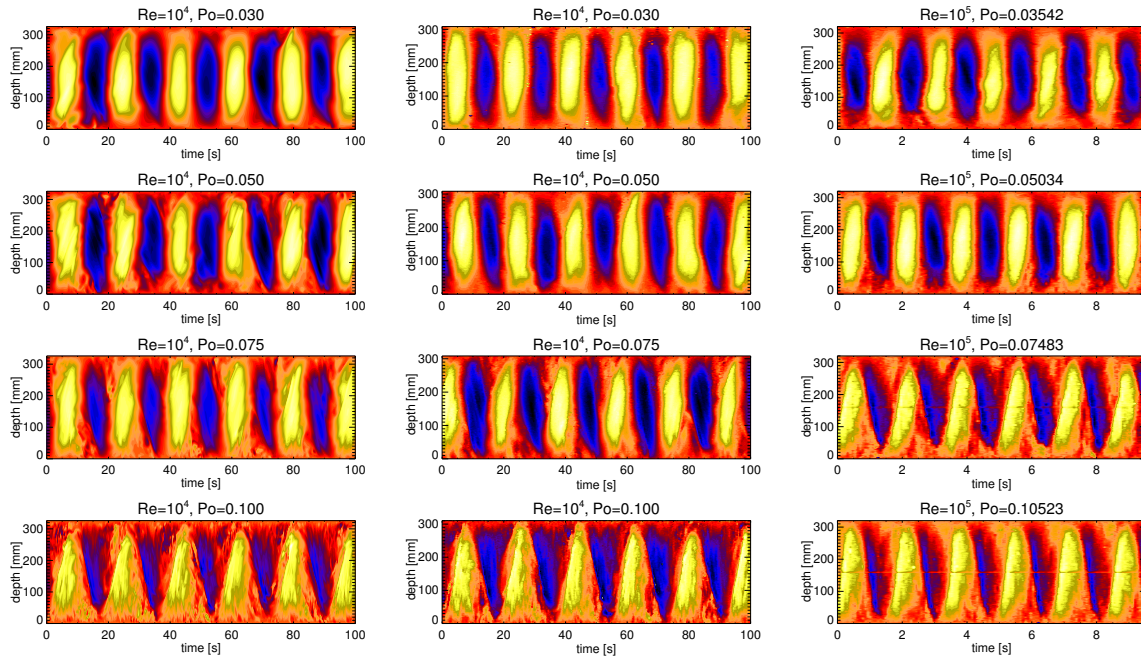


Figure 5. Velocity pattern for Re $= 10^4$ (left and center) and Re $= 10^5$ (right). From top to bottom: Po $= 0.03, 0.05, 0.075, 0.10$. The left column shows results from numerical simulations and the central and the right column show results from experimental measurements (colour online).

Typical flow patterns obtained in simulations and/or experiments are shown in figure 5. The plots present the evolution of the axial profile of the axial velocity $u_z(z)$ versus time $t$ at a fixed point in a co-rotating reference frame. The left column shows the results from simula-

tions at Re $= 10^4$, and the central and the right column show the results from experimental measurements (at Re $= 10^4$ and Re $= 10^5$, respectively). The alternating pattern with particular periodicity determined by the rotation frequency of the cylinder denotes the fundamental forced mode, the standing inertial wave with $(m, k) = (1, 1)$ sampled by the rotating probe which is attached to the container wall.

Above a certain precession ratio the fundamental pattern changes and the dominant structures exhibit a considerable tilt with respect to the vertical axis. This tilt is the implication of other inertial modes – in particular $(m, k) = (2, 2)$ and $(m, k) = (0, 2)$. The transition occurs at a critical precession ratio Po$^c$ which in turn depends on the Reynolds number. A further characteristic that changes at this transition is the amplitude of the directly driven mode, which decreases abruptly.

### 3.3.  *Spectra and amplitudes*

Quantitative values for these amplitudes are obtained from the spectra of individual inertial modes $(m, k)$ that are computed by a decomposition of the axial velocity profile in $z$ direction according to the typical dependence of an analytical inertial wave which behaves $\propto \sin(\pi zk/H)$. At a fixed timestep $t_n$ a $k$-mode $\tilde{u}_z^k$ (with the axial wave number $k$ being an integer) is calculated from the discretized data according to

$$\tilde{u}_z^k(r, \varphi_j, t_n) \,=\, \frac{1}{N_z} \sum_{l=0}^{N_z-1} u_z(r, \varphi_j, z_l, t_n) \, \sin\!\left(\frac{k\pi z_l}{H}\right), \tag{6}$$

where the radial coordinate $r$ is fixed at $r = 0.92$, the position of the UDV sensor in the experiment, and $\varphi_j, z_l, t_n$ are the discretized values for azimuthal coordinate, axial coordinate and time taken from the simulations. The axial modes $\tilde{u}_z^k$ are further decomposed by performing a 2D Fourier transformation in azimuth and in time with the resulting amplitudes characterized by the azimuthal wave number $m$ and the frequency $\omega$. This transformation explicitly reads

$$\tilde{\tilde{u}}_z^{km\omega}(r) \,=\, \frac{1}{N_\varphi N_t} \sum_{n=0}^{N_t-1} \sum_{j=0}^{N_\varphi-1} \tilde{u}_z^k(r, \varphi_j, t_n) \, e^{-i(m\varphi_j + \omega t_n)}. \tag{7}$$

The decomposition (7) involves a 2D FFT, which provides the amplitude spectrum for modes with fixed $m$ and $k$ in dependence of the frequency $\omega$ including the sign of $\omega$ that allows the distinction of prograde $(+)$ and retrograde $(-)$ components.

Figure 6 shows characteristic spectra for the dominant modes obtained from simulations at Re $= 10^4$ and Po $= 0.01, 0.03, 0.05, 0.875, 0.10, 0.125$ (from top to bottom). In these plots we switch from the mantle system into the turntable system in which the observer follows the precession and looks at the spinning cylinder. This means that a mode that in the mantle frame rotates with the frequency of the container, as it is the case for the directly forced flow, has the frequency $\omega = 0$ in the turntable frame thus being a standing wave. The reason for the change of the reference frame becomes clear when regarding the spectra of individual modes in figure 6, which are always dominated by one single peak located at $\omega = 0$. Thus, the main contribution of the flow results from modes that are stationary in the turntable reference frame.

The flow field is always dominated by the primary forced mode $(m, k) = (1, 1)$ which is directly excited by the Poincaré force. This is the directly forced standing inertial mode with $(m, k) = (1, 1)$. Higher modes, i.e., the modes with $(m, k) = (2, 2)$ (second column) result from nonlinear self-interaction of the direct forced mode. In principle, other modes with $(m, k) = (3, 3), (4, 4), \ldots$ (and so on) or Kelvin modes that may be directly forced (e.g. $(m, k) = (1, 3), (1, 5), ...$) can also be observed. However, their amplitudes are smaller and the
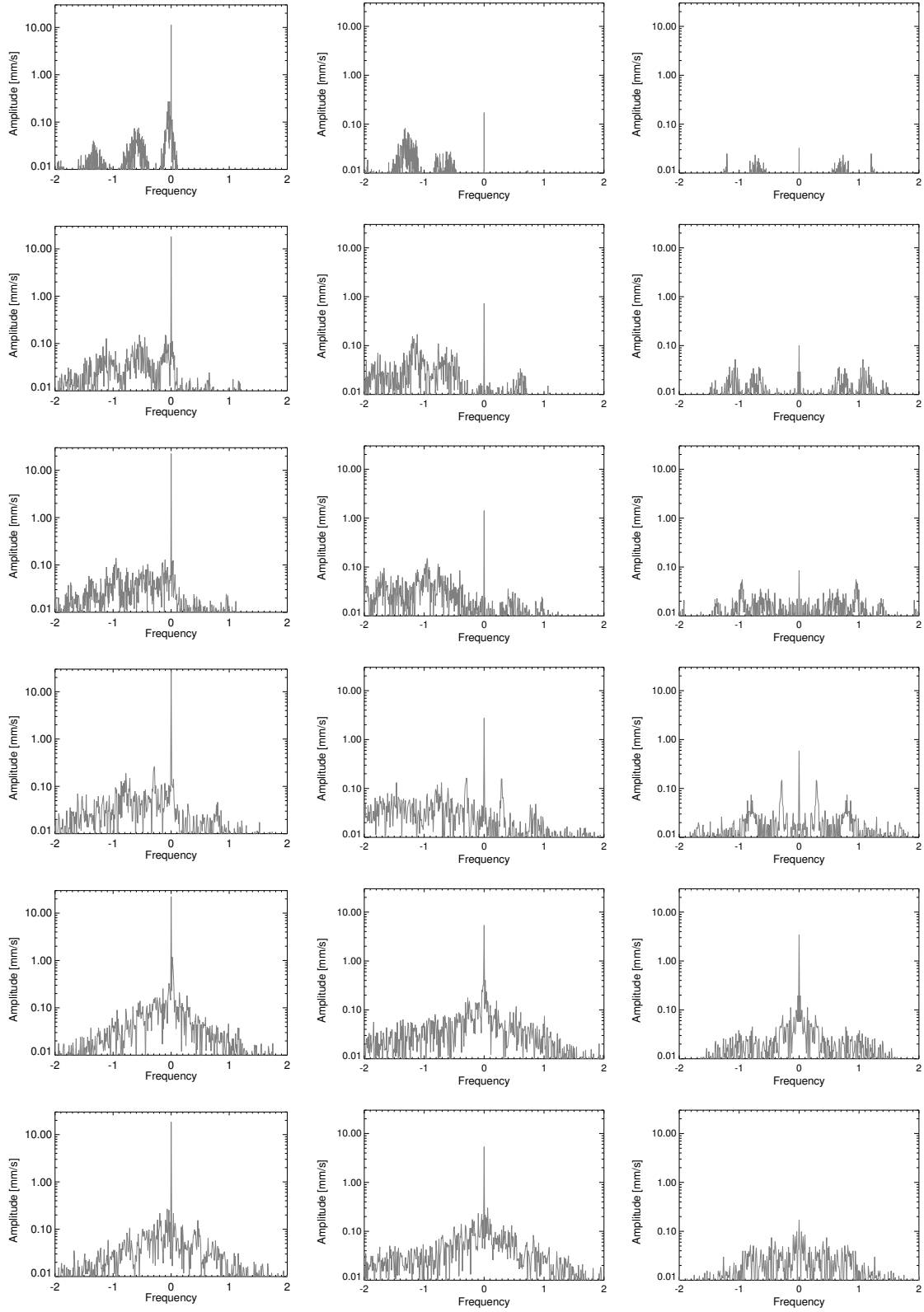
Figure 6. Spectra for Re $=$ $10^4$ from simulations at $r$ $=$ $0.92R$. From top to bottom: Po $=$ $0.01, 0.03, 0.05, 0.075, 0.10, 0.125$. From left to right: $(m, k) = (1, 1), (2, 2), (0, 2)$
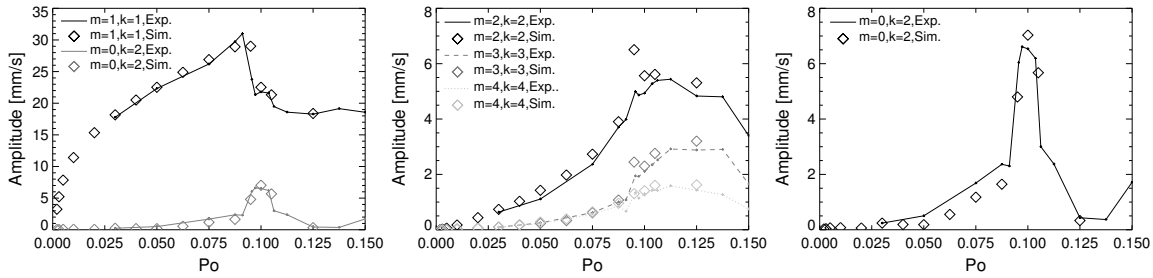
Figure 7. Amplitudes of the most dominant inertial modes from simulations (diamonds) and UDV measurements (solid curves) versus precession ratio. (a) $(m, k) = (1, 1)$ (black curve) and $(m, k) = (0, 2)$ (grey curve) (b) $(m, k) = (2, 2)$ (black curve), $(m, k) = (3, 3)$ (dark dashed grey curve) and $(m, k) = (4, 4)$ (light dotted grey curve) (c) close up of $(m, k) = (0, 2)$

most dominant modes are those presented in figure 6.

For small Po (i.e. Po = 0.01 and Po = 0.03) weak broad peaks with $\omega \neq 0$ can be recognized. In these regimes temporal variations in terms of irregularly appearing azimuthally drifting vortices emerge parallel to the cylinder axis. However, these features remain intermittent and do not show a strong amplitude. Similar features have been found experimentally (Mouhali *et al.* 2012) and numerically (Lin *et al.* 2016). For small precession ratios we also see weak broad maxima in the negative part of the spectrum which may indicate inertial waves propagating in the retrograde direction. However, these peaks are too weak and the maxima remain too broad so that so far no conclusion is possible about the nature of these features. Another less striking feature are the little peaks located symmetrically around the central peak in the runs at Po = 0.075 (fourth row). These peaks result from a periodic variation of the amplitude of the dominant mode. Again the corresponding amplitudes are weak and we will ignore these contributions in the following.

A much more noticeable peculiarity, which turns out to be important for the dynamo experiment, appears in the spectra shown in the right column that corresponds to an axisymmetric mode with $(m, k) = (0, 2)$. The amplitude of this mode is mostly small, except around Po $\approx 0.100$ where it becomes a significant contribution to the total flow (right plot in figure 7). In summary, the inspection of the spectra demonstrates that the precession driven flow in the turntable system is essentially dominated by standing inertial waves (Kelvin modes) and fluctuations do not play an important role. This is in particular valid for strongly precessing fluids. In the following, we ignore the time-dependent contributions and only discuss the amplitudes of modes that are standing in the turntable reference frame and have the frequency $\omega = 0$. The amplitudes of the most important inertial modes are shown in figure 7. The plots show the data obtained from simulations and experiments at Re = $10^4$. The left plot compares the directly forced mode $(m, k) = (1, 1)$ (black curve) and the axisymmetric mode $(m, k) = (0, 2)$ (grey curve), the central plot shows the corresponding behavior of the most important multiples excited from nonlinear self-interactions, $(m, k) = (2, 2)$ (black curve), $(m, k) = (3, 3)$ (grey curve), and $(m, k) = (4, 4)$ (light grey curve), and the right panel shows a close up of the behavior of the axisymmetric mode $(m, k) = (0, 2)$. In all cases simulations and experiments agree reasonable well (the diamonds denote simulations and the solid curves denote experimental data).

The plots in figure 7 illustrate the two essential characteristics of the flow amplitudes around Po = 0.1, which are the abrupt decrease of the amplitude of the $m = 1$ mode and the simultaneous emergence of the axially symmetric mode with $(m, k) = (0, 2)$ in the range $0.095 \lesssim$ Po $\lesssim 0.105$. In the meridional plane, the structure of the axially symmetric mode corresponds to a double roll pattern as it is shown in figure 8 which presents the poloidal flow
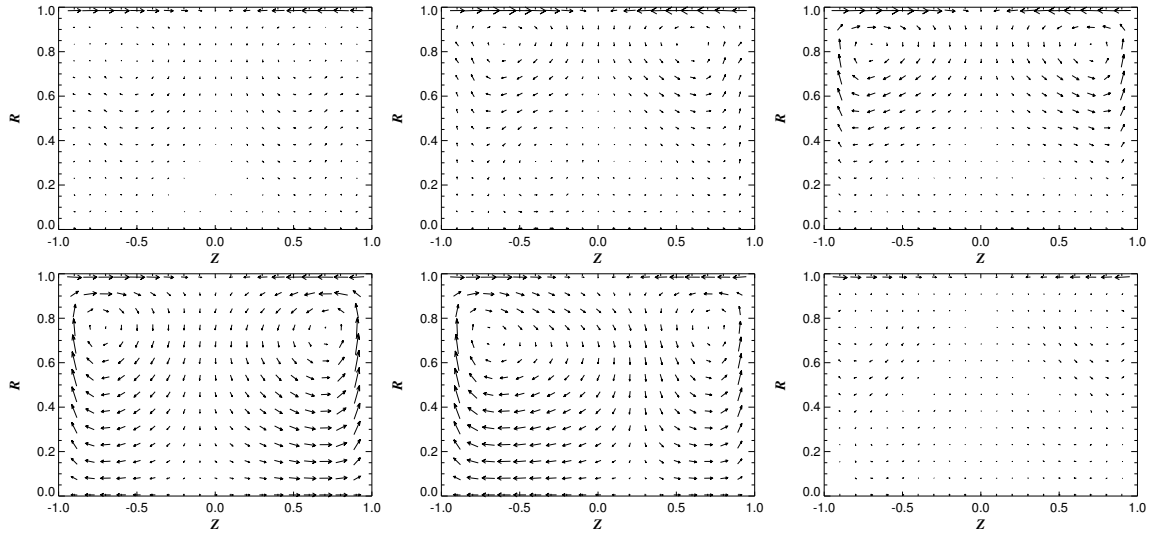
Figure 8. Structure of the poloidal components $u_r$ and $u_z$ of the time-averaged axisymmetric velocity field for various precession ratios. From top left to bottom right: Po = $0.05, 0.0875, 0.095, 0.100, 0.105, 0.125$.

components ($u_r$ and $u_z$) for different precession ratios. The double roll pattern only appears in the range Po $\in [0.095, 0.105]$ (figure 8(c), (d), (e)) with the clearest formation at Po = 0.100 where the rolls occupy almost the entire volume.

Regarding the mean azimuthal axisymmetric flow, we find that the modification of the initial solid body rotation continuously increases with Po. This change, shown in figure 9, is described by a circulation flow that is largely independent of $z$ and oriented opposite to the rotation of the container thus corresponding to a slowdown of the – initial – solid body rotation. Note also the change in the structure of this induced azimuthal flow. While there are two maxima close to the end caps for smaller Po, there is only one maximum in the equatorial plane for larger precession ratios.
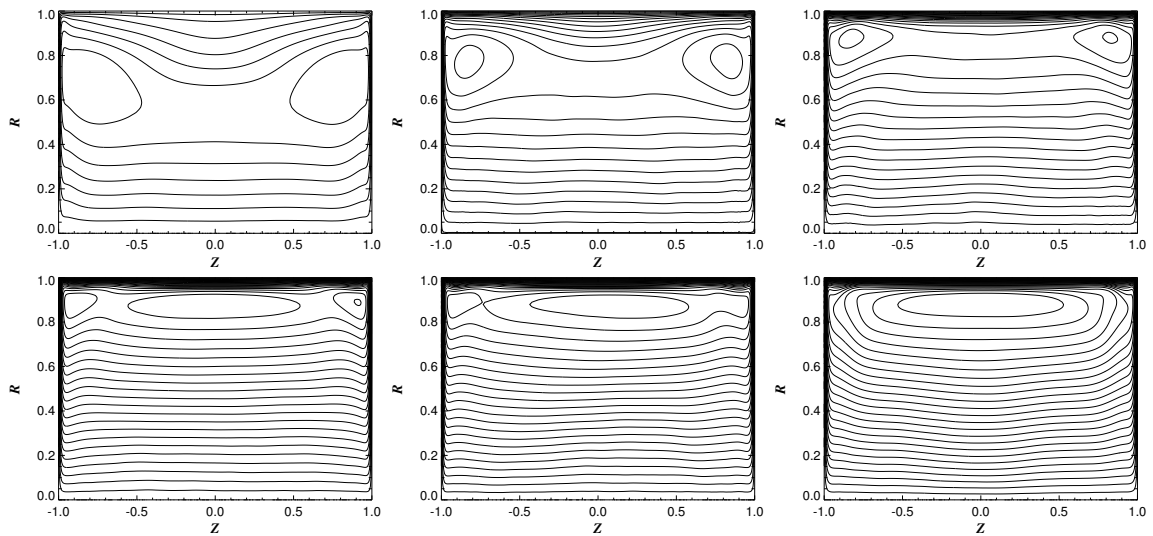


Figure 9. Structure of the time-averaged axisymmetric azimuthal velocity $u_\varphi$ without solid body rotation for various precession ratios. From top left to bottom right: Po = $0.05, 0.0875, 0.095, 0.100, 0.105, 0.125$.
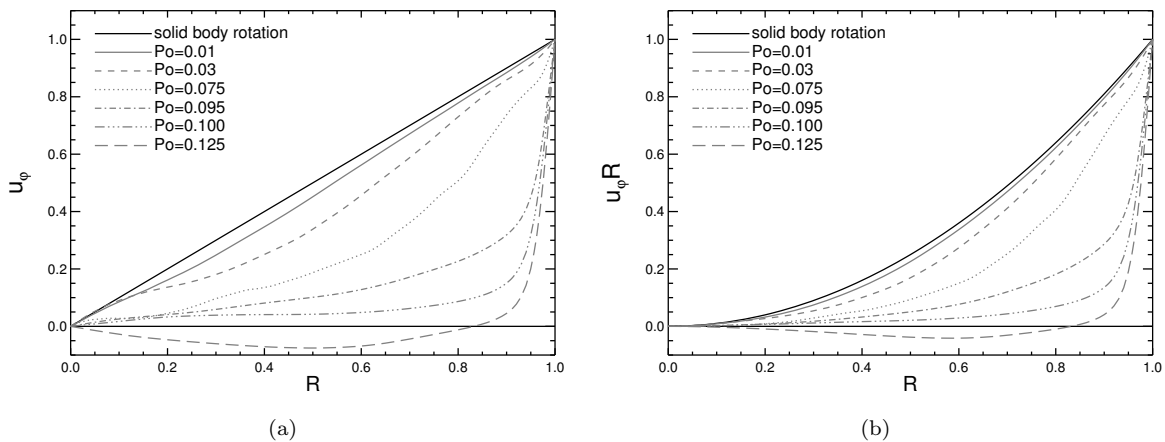
Figure 10.   (a) Radial profile of the azimuthal axisymmetric velocity $u_\varphi$ including the solid body rotation from simulations with various precession ratios at $\mathrm{Re} = 10^4$. (b) Corresponding profiles of the angular momentum.

### 3.4.   *A centrifugal instability*

The change in the azimuthal circulation described in the previous section is surprisingly strong and is supposed to be the reason for the occurrence of the double roll flow which is reminiscent of the vortices arising in a Taylor Couette setup. The *induced* azimuthal velocity is nearly independent of the axial coordinate and oriented opposite to the solid body rotation that would exist in a pure rotating system without precessional forcing. This slowdown of the solid body rotation increases with the precession ratio Po such that nearly exactly at the critical point, i.e. at Po $\sim$ 0.1, the Rayleigh criterion for the stability of a rotating fluid becomes violated. This can be seen in figure 10 which shows the radial profile of $u_\varphi$ (left) and the corresponding angular momentum $ru_\varphi$ (right) for increasing Po including the solid body rotation. The slope of the angular momentum is indeed negative in the bulk when Po $\gtrsim$ 0.1 which is the criterion for the occurrence of a centrifugal instability. In the specific case of the azimuthal velocity profiles as they are generated by precession, the axisymmetric double roll structure occurs shortly before reaching the Rayleigh line, which can be explained by the presence of the strong $m = 1$ mode due to the direct precessional forcing. A more detailed investigation would therefore require a stability analysis of the superposition of the induced circulation and the directly driven Kelvin mode. Since this is not straightforward – and probably requires the additional consideration of boundary layers that are not well known, we postpone such an calculation to a future study.

### 3.5.   *Dependence on Reynolds number*

Whereas numerical simulations are limited to Re $\lesssim 10^4$, UDV measurements in the water experiment are possible up to Re $= 10^5$. The results show that the essential characteristics of the flow behavior in dependence of the precession ratio hardly change. This can be seen in figure 5 for the total flow, and for the axisymmetric flow in figure 11(a) which shows the axial profile of the time-average of $u_z$ versus $z$ measured with UDV at $r = 0.9R$. The flow profiles are scaled by the respective maximum value so that all curves roughly collapse, indicating that only minor changes of the flow structure appear when increasing Re.

An exception is the critical value for the precession ratio Po$^c$ at which the axisymmetric mode emerges and the amplitude of the directly forced flow drops (left plot in figure 11). Po$^c$ decreases with increasing Re, however, the reduction of Po$^c$ mainly takes place for Re $\lesssim 4 \times 10^4$ (from Po$^c \approx 0.100$ at Re $= 10^4$ to Po$^c \approx 0.075$ at Re $= 4 \times 10^4$). Further increasing Re, the
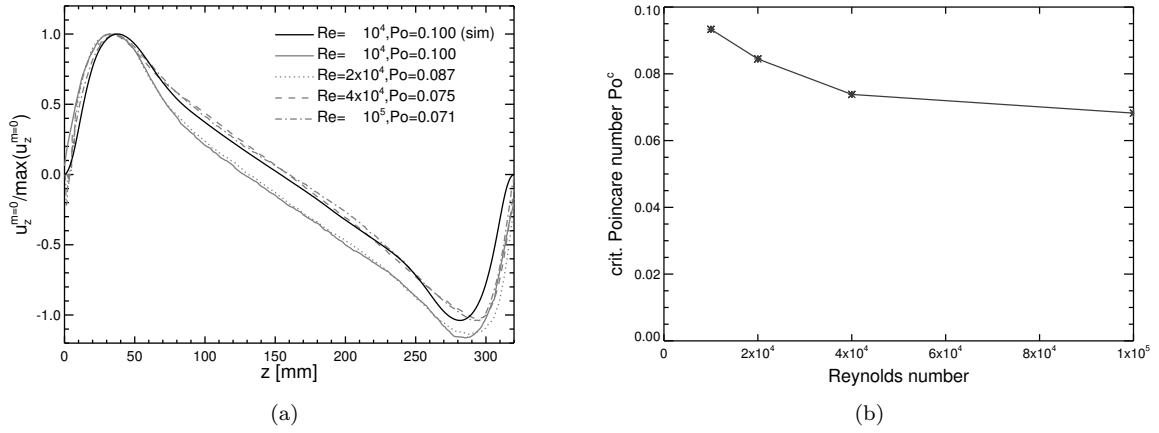
Figure 11.   (a) Axial profile of the axisymmetric part of $u_z$ for various Re scaled by the respective maximum. (b) Critical value for the precession ratio Po$^{\mathrm{c}}$ at which the axisymmetric mode $(m, k) = (0, 2)$ emerges.

measurements indicate an asymptotic behavior with a saturation around Po$^{\mathrm{c}} \approx 0.07$. This is supported by measurements of the pressure fluctuations at the end caps presented in Herault *et al.* (2015). These pressure measurements provide the precession ratio at which the amplitude of the $m = 1$ mode drops abruptly but give only little information on the very flow structure or the contributing modes. The pressure data is available up to Re $\approx 2 \times 10^6$ and shows that nearly no further change of Po$^{\mathrm{c}}$ occurs up to this value of the Reynolds number. However, these measurements can only be regarded as a hint for the behavior of Po$^{\mathrm{c}}$, and further experiments in the intermediate regime – in particular with better information on the flow structure – are required.

## 4.    The kinematic dynamo problem

### 4.1.    *Growth rates*

In order to deduce whether a precessing conducting liquid is capable to sustain a magnetic field we run simulations of the magnetic induction equation which describes the temporal evolution of the magnetic field $\boldsymbol{B}$ and reads

$$\frac{\partial \boldsymbol{B}}{\partial t} = \boldsymbol{\nabla} \times \bigl(\boldsymbol{u} \times \boldsymbol{B} - \eta \boldsymbol{\nabla} \times \boldsymbol{B}\bigr). \tag{8}$$

Since we have seen in the previous sections that the dominant contribution of the fluid flow is essentially stationary in the turntable reference frame, we revert to the kinematic approach and apply the time-averaged velocity field obtained from our hydrodynamic simulations. An advanced model would include turbulent fluctuations on top of the stationary flow. It is well known that such contributions may inhibit dynamo action (Pétrélis and Fauve 2006, Pétrélis *et al.* 2007) because these fluctuations cause an decrease of the effective electrical conductivity ($\beta$-effect). However, experiments at the Riga dynamo facility where a turbulence level of roughly 7% on top of the flow was observed, showed that the restriction to a simple laminar flow model is sufficient to describe the onset of dynamo action in this experimental system (Gailitis *et al.* 2000, 2004, 2008). We thus suppose that temporal fluctuations of the flow field only have a minor impact for the onset of dynamo action, at least in the regime that is relevant for the present study.

We utilize different time-averaged velocity fields obtained from hydrodynamic simulations at Re $= 10^4$ and various Po. The magnetic induction equation (8) is solved numerically using
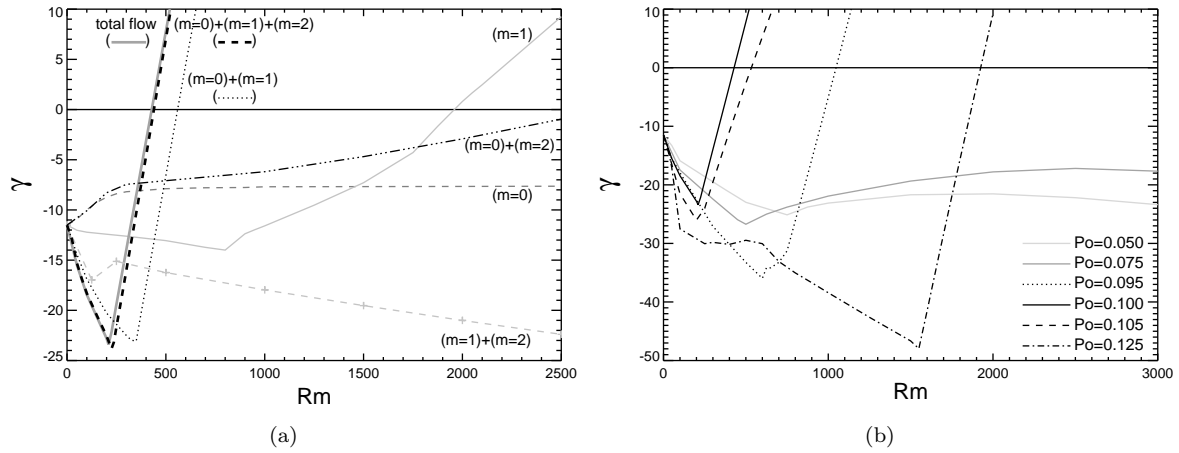
Figure 12. (a) Magnetic field growth rates versus Rm induced by various combinations of individual azimuthal flow modes of the hydrodynamic flow obtained at Re $= 10^4$ and Po $= 0.1$. (b) Magnetic field growth rates versus Rm induced by the time-averaged total flow obtained at Re $= 10^4$ and various precession ratios Po.

a finite volume scheme with constraint transport in order to ensure $\boldsymbol{\nabla}\cdot\boldsymbol{B} = 0$ (Giesecke *et al.* 2008). For all simulations we apply pseudo-vacuum boundary conditions for the magnetic field, i.e. at the boundary the tangential field components vanish. This behavior mimics an exterior domain with infinite permeability and it is known from numerical simulations for the von-Kármán-Sodium dynamo that these boundary conditions may have a beneficial impact for dynamo action (Giesecke *et al.* 2010, see also section 4.2 below).

For the particular case Re $= 10^4$ and Po $= 0.1$ we decompose the flow field into different azimuthal modes with $m = 0, m = 1, m = 2$ and compute solutions of multiple combinations of these individual contributions. Figure 12(a) shows that the axisymmetric flow alone $(m = 0)$ is not able to drive a dynamo, and although the cases $(m = 1)$ and $(m = 0) + (m = 2)$ show a positive growth rate – and thus provide a dynamo – this only happens at relatively large magnetic Reynolds numbers Rm $= \Omega_c R^2/\eta$, which will not be achievable in the experiment. A critical magnetic Reynolds numbers sufficiently low for the planned experiment is only obtained when considering at least the directly forced flow and the axisymmetric flow, i.e., $(m = 0) + (m = 1)$ (dotted curve in figure 12(a)).

We conclude that the best way to drive the dynamo is attained from the largest scales of the velocity field and there is nearly no difference in the growth rates between dynamos driven by a velocity field consisting only of the $m = 0, m = 1$ and $m = 2$ mode (dashed black curve) and dynamos that are driven by the full (time-averaged) velocity field (solid grey curve).

Finally, we briefly discuss the results obtained with the total flow field obtained from the hydrodynamic simulations at different precession ratios Po with the Reynolds number fixed at Re $= 10^4$. Figure 12(b) shows the magnetic energy growth rates for the cases Po $= 0.05, 0.075, 0.095, 0.100, 0.105$, and Po $= 0.125$. We find dynamos only for flows obtained for Po $> 0.075$ (see table 1). However, the critical value for Rm$^c$ is only within the regime that will be achievable in the dynamo experiment when using velocity fields obtained around Po $\approx 0.100$, i.e. when the axisymmetric double roll structure is present (bold numbers in table 1). The minimum value for Rm$^c$ is found with the velocity field obtained at Re $= 10^4$

| Po | 0.05 | 0.075 | 0.0875 | **0.095** | **0.100** | **0.105** | 0.125 |
|---|---|---|---|---|---|---|---|
| Rm$^c$ | $> 5000$ | $> 5000$ | $\sim 4900$ | **1045** | **430** | **530** | 1930 |

Table 1. Critical magnetic Reynolds number for various precession ratios. For Po $= 0.05$ and Po $= 0.075$ we did not find dynamos up to Rm $= 5000$ and the development of the growthrates suggest that these flows do not show dynamo action at all. The bold numbers denote the cases with Rm$^c$ in the range of experimentally achievable values.

and Po $= 0.100$ where the relation of the axisymmetric mode $(m, k) = (0, 2)$ to the directly forced mode $(m, k) = (1, 1)$ has its maximum value. A common feature for all cases is the strong initial decrease of the growth rates when increasing Re. This behavior changes abruptly at a certain value of Rm at which the growth rates begin to increase with a rather steep slope. The sudden change goes along with a change in the temporal behavior of the magnetic field. Whereas the solution is stationary in the regime with decreasing growth rate, behind the sudden bent the magnetic field has an oscillatory contribution. However, the main part of the magnetic field is constant in time with the eigenmode performing a rotation around the symmetry axis of the cylinder (figure 13).

## 4.2.    *Magnetic boundary conditions*

In the following, we will concentrate on the behavior of the magnetic field for the case Po $= 0.100$ for which we obtain the smallest $Rm^c$. An important issue that determines self-excitation of magnetic fields is the impact of the electrical boundary conditions for which pseudo vacuum conditions (i.e. vanishing tangential fields) have been utilized. In the planned experiment the container will be made of stainless steel with a magnetic permeability very close to $\mu_r = 1$ but with an magnetic diffusivity that at a typical operating temperature of $T \approx 120°$C is roughly a factor six larger than the diffusivity of liquid sodium. In that case the solution for the magnetic field – in particular its growth rate – is affected by the material properties of the container, i.e., its magnetic diffusivity $\eta_{\text{wall}}$ and its thickness $d_{\text{wall}}$, whereas the electric properties of the very outer regime remain less important. We extend our previous dynamo models by including an outer shell with thickness $d_{\text{wall}} = 5$ cm. The real value in the planned dynamo experiment will be $d_{\text{wall}} = 3$ cm, but for numerical reasons we seek to consider a sufficient number of grid cells that represent the container wall. Within the wall the "flow" is prescribed by a solid body rotation, and the magnetic diffusivity $\eta_{\text{wall}}$ may differ from the diffusivity in the fluid domain. We find two different dynamo states that are distinguished by the container diffusivity (figure 14). For $\eta_{\text{wall}}/\eta \lesssim 2$ the critical magnetic Reynolds number is large and remains far above values that will be achievable in the planned experiment. Above $\eta_{\text{wall}}$, however, $Rm^c$ drops significantly, and remains nearly independent of $\eta_{\text{wall}}$ with $Rm^c \approx 450$ for the realistic case $\eta_{\text{wall}} = 6\eta$. It is surprising that the structure of the magnetic field in both regimes is quite
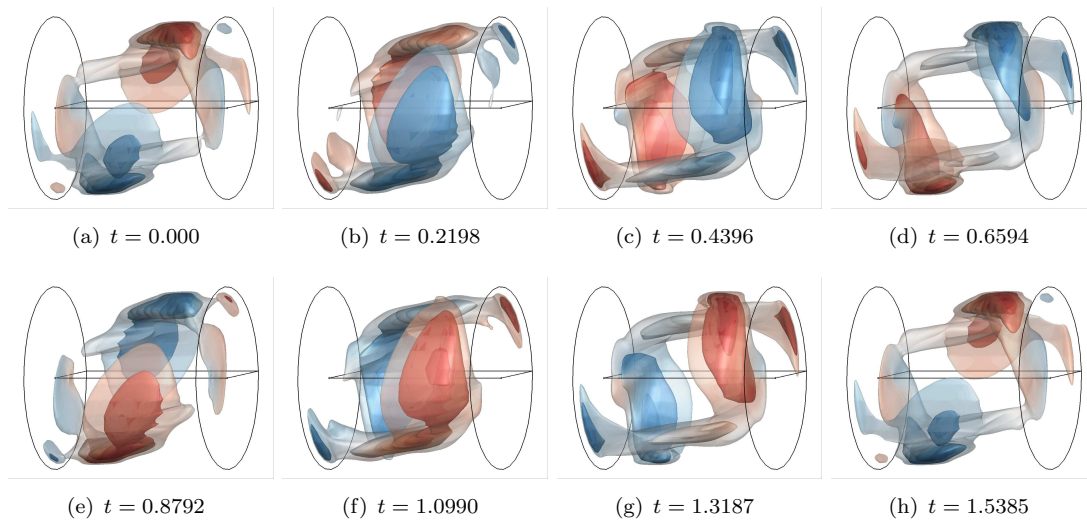


(a) $t = 0.000$      (b) $t = 0.2198$      (c) $t = 0.4396$      (d) $t = 0.6594$

(e) $t = 0.8792$      (f) $t = 1.0990$      (g) $t = 1.3187$      (h) $t = 1.5385$

Figure 13.    Magnetic energy density at $10, 25, 50\%$ of the maximum value mapped with the azimuthal field $B_\varphi$. Rm $= 450$. The time-averaged flow field results from hydrodynamic simulations at Re $= 10^4$ and Po $= 0.1$. The time is denoted in units of the rotation time (colour online).

similar, and that without an outer shell the simplifying pseudo-vacuum boundary conditions emulate the impact of container walls with increased diffusivity.

Less unusual is the sensitivity of the solution to small variations in the diffusivity of this outer shell, which is a typical property of boundary eigenvalue problems of simple dynamo models (Kirillov *et al.* 2009). In connection with the abrupt and sharp change of the growth rates and the transition from time-independent to oscillating solutions, this behavior suggests the presence of exceptional points. These points represent distinguished locations in the spectrum at which two degenerated solutions occur with equal eigenvalues and identical eigenvectors and are important ingredients for example in models of reversals of the geomagnetic field.

## 5.    Conclusions

Our kinematic dynamo models indicate that magnetic self-excitation by a precession driven flow in a cylindrical container may be possible in a narrow parameter regime that indeed will be achievable in the planned precession dynamo experiment at HZDR. This regime is essentially characterized by the presence of an axisymmetric double roll structure in the meridional plane. For small Re the critical precession ratio $Po^c$, at which the axisymmetric flow mode emerges, decreases with increasing Re. However, the UDV measurements at larger Re as well as the behavior of the pressure and the hysteresis deduced from the power consumption measured by Herault *et al.* (2015) suggest that for sufficiently large Re the critical precession ratio becomes largely independent of Re with values around $Po^c \approx 0.07$ when $Re \gtrsim 10^6$.

Nevertheless, it remains quite ambitious to scale the results obtained at comparable small Reynolds number $Re \sim 10^4$ to the large device, where, in order to reach the predicted critical values $Rm^c \approx 400\ldots500$, the fluid flow will correspond to Reynolds numbers of the order $O(10^7)$. Our investigations indicate that for $Po \lesssim Po^c$, i.e. before the transition into the turbulent regime, the flow is essentially quasi-laminar and does hardly change its structure when increasing Re. In particular the axisymmetric mode, which emerges immediately before the transition to the turbulent regime and which is a crucial ingredient for dynamo action at low Rm, does not vanish in the fast rotating case (i.e. large Re) so that there we have some basic confidence in the transferability of our results to the large dynamo experiment. The minimum value of the critical magnetic Reynolds number $Rm^c$ for the onset of dynamo action found in our dynamo models is $Rm^c \approx 430$. This value is obtained from kinematic dynamo simulations using the time-averaged velocity field computed in hydrodynamical simulations
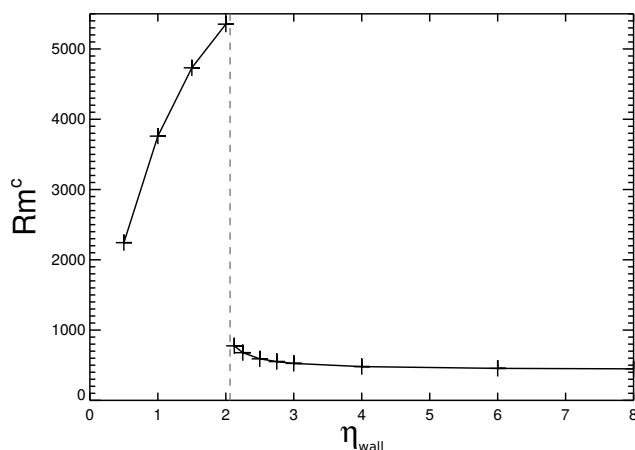


Figure 14.    Critical magnetic Reynolds number versus the diffusivity of the outer layer $\eta_{wall}$ with thickness $d_{wall} = 5$ cm. The flow field is the time-averaged field obtained in hydrodynamic simulations at $Re = 10^4$ and $Po = 0.1$.

at Re $= 10^4$ and Po $= 0.100$. Assuming that the flow structure – and therefore the dynamo capability – remains the same even for the large Re that will occur in the real experiment and that the critical value for the precession ratio $Po^c$ for the emergence of the axisymmetric mode will be around $Po^c \approx 0.07$ (as suggested by the behavior shown in figure 11(b)), we end up at a corresponding rotation frequency of $f_c \approx 6.8$ Hz and a precession frequency of $f_p \approx 0.5$ Hz that will be required for a dynamo in the planned experiment (assuming $\eta = 0.1$ m$^2$/s). In order to confirm this values, further studies are necessary that focus on the impact of electromagnetic boundary conditions and the influence of time-dependent flow contributions.

we may explicitly estimate the parameters that will be required in order to obtain magnetic field self-excitation in the liquid sodium experiment. This scaling would lead to a rotation frequency of $f_c \approx 6.8$ Hz and a precession frequency of $f_p \approx 0.5$ Hz

## References

Albrecht, T., Blackburn, H.M., Lopez, J.M., Manasseh, R. and Meunier, P., On triadic resonance as an instability mechanism in precessing cylinder flow. *J. Fluid Mech.*, 2018, **841**, R3.

Blackburn, H.M. and Sherwin, S.J., Formulation of a Galerkin spectral element-Fourier method for three-dimensional incompressible flows in cylindrical geometries. *J. Comp. Phys.*, 2004, **197**, 759–778.

Busse, F.H., Steady fluid flow in a precessing spheroidal shell. *J. Fluid Mech.*, 1968, **33**, 739–751.

Ernst-Hullermann, J., Harder, H. and Hansen, U., Finite volume simulations of dynamos in ellipsoidal planets. *Geophys. J. Int.*, 2011, **195**, 1395–1405.

Gailitis, A., Gerbeth, G., Gundrum, T., Lielausis, O., Platacis, E. and Stefani, F., History and results of the Riga dynamo experiments. *C. R. Phys.*, 2008, **9**, 721–728.

Gailitis, A., Lielausis, O., Dement'ev, S., Platacis, E., Cifersons, A., Gerbeth, G., Gundrum, T., Stefani, F., Christen, M., Hänel, H. and Will, G., Detection of a Flow Induced Magnetic Field Eigenmode in the Riga Dynamo Facility. *Phys. Rev. Lett.*, 2000, **84**, 4365–4368.

Gailitis, A., Lielausis, O., Platacis, E., Gerbeth, G. and Stefani, F., Riga dynamo experiment and its theoretical background. *Phys. Plasmas*, 2004, **11**, 2838–2843.

Gans, R.F., On the precession of a resonant cylinder. *J. Fluid Mech.*, 1970, **41**, 865–872.

Gans, R.F., On hydromagnetic precession in a cylinder. *J. Fluid Mech.*, 1971, **45**, 111–130.

Giesecke, A., Albrecht, T., Gundrum, T., Herault, J. and Stefani, F., Triadic resonances in nonlinear simulations of a fluid flow in a precessing cylinder. *New J. Phys.*, 2015, **17**, 113044.

Giesecke, A., Nore, C., Stefani, F., Gerbeth, G., Leorat, J., Luddens, F. and Guermond, J.L., Electromagnetic induction in non-uniform domains. *Geophys. Astrophys. Fluid Dyn.*, 2010, **104**, 505–529.

Giesecke, A., Stefani, F. and Gerbeth, G., Kinematic simulation of dynamo action by a hybrid boundary-element/finite-volume method. *Magnetohydrodynamics*, 2008, **44**, 237–252.

Giesecke, A., Vogt, T., Gundrum, T. and Stefani, F., Nonlinear Large Scale Flow in a Precessing Cylinder and Its Ability To Drive Dynamo Action. *Phys. Rev. Lett.*, 2018, **120**, 024502.

Goepfert, O. and Tilgner, A., Dynamos in precessing cubes. *New J. Phys.*, 2016, **18**, 103019.

Goto, S., Ishii, N., Kida, S. and Nishioka, M., Turbulence generator using a precessing sphere. *Phys. Fluids*, 2007, **19**, 061705–061705.

Goto, S., Matsunaga, A., Fujiwara, M., Nishioka, M., Kida, S., Yamato, M. and Tsuda, S., Turbulence driven by precession in spherical and slightly elongated spheroidal cavities. *Phys. Fluids*, 2014, **26**, 055107.

Greenspan, H.P., *The theory of rotating fluids*, 1968 (Cambridge University Press).

Greenspan, H.P., On the non-linear interaction of inertial modes. *J. Fluid Mech.*, 1969, **36**, 257–264.

Herault, J., Giesecke, A., Gundrum, T. and Stefani, F., Instability of precession driven Kelvin modes: evidence of a detuning effect. *ArXiv e-prints*, 2018 Submitted to Phys. Rev. Fluids.

Herault, J., Gundrum, T., Giesecke, A. and Stefani, F., Subcritical transition to turbulence of a precessing flow in a cylindrical vessel. *Phys. Fluids*, 2015, **27**, 124102.

Herreman, W., Instabilité elliptique sous champ magnétique & Dynamo d'ondes inertielles. Ph.D. Thesis, Université de Provence Aix-Marseille I, Insitut de Recherche sur les Phénomènes Hors Équilibre Https://tel.archives-ouvertes.fr/tel-00452471/document, 2009.

Hollerbach, R. and Kerswell, R.R., Oscillatory internal shear layers in rotating and precessing flows. *J. Fluid Mech.*, 1995, **298**, 327–339.

Horimoto, Y. and Goto, S., Sustaining mechanism of small-scale turbulent eddies in a precessing sphere. *Physical Review Fluids*, 2017, **2**, 114603.

Horimoto, Y., Simonet-Davin, G., Katayama, A. and Goto, S., Impact of a small ellipticity on the sustainability condition of developed turbulence in a precessing spheroid. *Phys. Rev. Fluids*, 2018, **3**, 044603.

Kerswell, R.R., The instability of precessing flow. *Geophys. Astrophys. Fluid Dyn.*, 1993, **72**, 107–144.

Kirillov, O.N., Günther, U. and Stefani, F., Determining role of Krein signature for three-dimensional Arnold tongues of oscillatory dynamos. *Phys. Rev. E*, 2009, **79**, 016205.

Kobine, J.J., Inertial wave dynamics in a rotating and precessing cylinder. *J. Fluid Mech.*, 1995, **303**, 233–252.

Kobine, J.J., Azimuthal flow associated with inertial wave resonance in a precessing cylinder. *J. Fluid Mech.*, 1996, **319**, 387–406.

Lagrange, R., Meunier, P., Nadal, F. and Eloy, C., Precessional instability of a fluid cylinder. *J. Fluid Mech.*, 2011, **666**, 104–145.

Léorat, J., Large scales features of a flow driven by precession. *Magnetohydrodynamics*, 2006, **42**, 143–151.

Léorat, J., Rigaud, F., Vitry, R. and Herpe, G., Dissipation in a flow driven by precession and application to the design of a MHD wind tunne. *Magnetohydrodynamics*, 2003, **39**, 321–326.

Liao, X. and Zhang, K., On flow in weakly precessing cylinders: the general asymptotic solution. *J. Fluid Mech.*, 2012, **709**, 610–621.

Lin, Y., Marti, P., Noir, J. and Jackson, A., Precession-driven dynamos in a full sphere and the role of large scale cyclonic vortices. *Phys. Fluids*, 2016, **28**, 066601.

Lin, Y., Noir, J. and Jackson, A., Experimental study of fluid flows in a precessing cylindrical annulus. *Phys. Fluids*, 2014, **26**, 046604.

Lopez, J.M. and Marques, F., Nonlinear and detuning effects of the nutation angle in precessionally forced rotating cylinder flow. *Phys. Rev. Fluids*, 2016, **1**, 023602.

Lorenzani, S. and Tilgner, A., Fluid instabilities in precessing spheroidal cavities. *J. Fluid Mech.*, 2001, **447**, 111–128.

Lorenzani, S. and Tilgner, A., Inertial instabilities of fluid flow in precessing spheroidal shells. *J. Fluid Mech.*, 2003, **492**, 363–379.

Malkus, W.V.R., Precession of the Earth as the Cause of Geomagnetism. *Science*, 1968, **160**, 259–264.

Manasseh, R., Breakdown regimes of inertia waves in a precessing cylinder. *J. Fluid Mech.*, 1992, **243**, 261–296.

Manasseh, R., Distortions of inertia waves in a rotating fluid cylinder forced near its fundamental mode resonance. *J. Fluid Mech.*, 1994, **265**, 345–370.

Marques, F. and Lopez, J.M., Precession of a rapidly rotating cylinder flow: traverse through resonance. *J. Fluid Mech.*, 2015, **782**, 63–98.

McEwan, A.D., Inertial oscillations in a rotating fluid cylinder. *J. Fluid Mech.*, 1970, **40**, 603–640.

Meunier, P., Eloy, C., Lagrange, R. and Nadal, F., A rotating fluid cylinder subject to weak precession. *J. Fluid Mech.*, 2008, **599**, 405–440.

Mouhali, W., Lehner, T., Léorat, J. and Vitry, R., Evidence for a cyclonic regime in a precessing cylindrical container. *Exp. Fluids*, 2012, **53**, 1693–1700.

Noir, J., Brito, D., Aldridge, K. and Cardin, P., Experimental evidence of inertial waves in a precessing spheroidal cavity. *Geophys. Res. Lett.*, 2001a, **28**, 3785–3788.

Noir, J., Cardin, P., Jault, D. and Masson, J.P., Experimental evidence of non-linear resonance effects between retrograde precession and the tilt-over mode within a spheroid. *Geophys. J. Int.*, 2003, **154**, 407–416.

Noir, J. and Cébron, D., Precession-driven flows in non-axisymmetric ellipsoids. *J. Fluid Mech.*, 2013, **737**, 412–439.

Noir, J., Jault, D. and Cardin, P., Numerical study of the motions within a slowly precessing sphere at low Ekman number. *J. Fluid Mech.*, 2001b, **437**, 283–299.

Nore, C., Léorat, J., Guermond, J.L. and Luddens, F., Nonlinear dynamo action in a precessing cylindrical container. *Phys. Rev. E*, 2011, **84**, 016317.

Pétrélis, F. and Fauve, S., Inhibition of the dynamo effect by phase fluctuations. *Europhys Lett.)*, 2006, **76**, 602–608.

Pétrélis, F., Mordant, N. and Fauve, S., On the magnetic fields generated by experimental dynamos. *Geophys. Astrophys. Fluid Dyn.*, 2007, **101**, 289–323.

Poincaré, H., Sur la précession des corps déformables. *Bulletin Astronomique*, 1910, **27**, 321–356.

Stefani, F., Eckert, S., Gerbeth, G., Giesecke, A., Gundrum, T., Steglich, C., Weier, T. and Wustmann, B., DRESDYN – a new facility for MHD experiments with liquid sodium. *Magnetohydrodynamics*, 2012, **48**, 103–114.

Stewartson, K. and Roberts, P.H., On the motion of a liquid in a spheroidal cavity of a precessing rigid body. *J. Fluid Mech.*, 1963, **17**, 1–20.

Thomson, W., Vibrations of a columnar vortex. *Philos. Mag.*, 1880, **10**, 152–165.

Tilgner, A., On models of precession driven core flow. *Studia geoph. et geod.*, 1998, **42**, 232–238.

Tilgner, A., Precession driven dynamos. *Phys. Fluids*, 2005, **17**, 034104.

Tilgner, A., Zonal Wind Driven by Inertial Modes. *Phys. Rev. Lett.*, 2007, **99**, 194501.

Vanyo, J.P., A geodynamo powered by luni-solar precession. *Geophys. Astrophys. Fluid Dyn.*, 1991, **59**, 209–234.

Vanyo, J.P. and Likins, P.W., Measurement of Energy Dissipation in a Liquid-Filled, Precessing, Spherical

Cavity. *J. Appl. Mech.*, 1971, **38**, 674.

Wu, C.C. and Roberts, P., On a dynamo driven by topographic precession. *Geophys. Astrophys. Fluid Dyn.*, 2009, **103**, 467–501.